

Laser powder bed fusion of a superelastic Cu-Al-Mn shape memory alloy

N. Babacan^{a,b,*}, S. Pauly^{a,c}, T. Gustmann^{a,**}

^a Leibniz Institute for Solid State and Materials Research Dresden (Leibniz IFW Dresden), Institute for Complex Materials, Dresden D-01069, Germany

^b Department of Mechanical Engineering, Sivas University of Science and Technology, Sivas 58140, Turkey

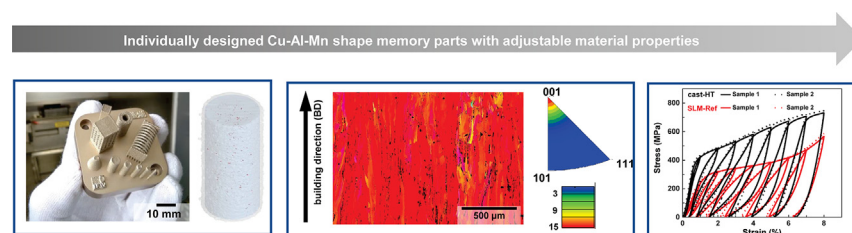
^c University of Applied Sciences Aschaffenburg, Aschaffenburg D-63743, Germany



HIGHLIGHTS

- High-density samples across a wide range of energy inputs were successfully produced via laser powder bed fusion (LPBF).
- High-quality Cu-Al-Mn parts with complex geometries could be fabricated by laser powder bed fusion.
- Transformation temperatures were tailored through tuning the LPBF process parameters.
- Additively manufactured samples showed higher superelastic strain compared to the cast samples at the room temperature.

GRAPHICAL ABSTRACT



ARTICLE INFO

Article history:

Received 2 December 2020

Received in revised form 6 February 2021

Accepted 27 February 2021

Available online 2 March 2021

Keywords:

Additive manufacturing

Laser powder bed fusion

Shape memory alloy

Cu-Al-Mn

Martensitic transformation

Superelasticity

ABSTRACT

Dense and crack-free specimens of the shape memory alloy $\text{Cu}_{71.6}\text{Al}_{17}\text{Mn}_{11.4}$ (at.%) were produced via laser powder bed fusion across a wide range of process parameters. The microstructure, viz. grain size, can be directly tailored within the process and with it the transformation temperatures (TTs) shifted to higher values by raising the energy input. The microstructure, and the superelastic behavior of additively manufactured samples were assessed by a detailed comparison with induction melted material. The precipitation of the α phase, which inhibit the martensitic transformation, were not observed in the additively manufactured samples owing to the high intrinsic cooling rates during the fabrication process. Fine columnar grains with a strong [001]-texture along the building direction lead to an enhanced yield strength compared to the coarse-grained cast samples. A maximum recoverable strain of 2.86% was observed after 5% compressive loading. The first results of our approach imply that laser powder bed fusion is a promising technique to directly produce individually designed Cu-Al-Mn shape memory parts with a pronounced superelasticity at room temperature.

© 2021 Published by Elsevier Ltd. This is an open access article under the CC BY-NC-ND license (<http://creativecommons.org/licenses/by-nc-nd/4.0/>).

* Corresponding author at: Department of Mechanical Engineering, Sivas University of Science and Technology, Sivas 58140, Turkey

** Corresponding author at: Leibniz Institute for Solid State and Materials Research Dresden (Leibniz IFW Dresden), Institute for Complex Materials, Dresden D-01069, Germany.

E-mail addresses: nazimbabacan@sivas.edu.tr (N. Babacan), t.gustmann@ifw-dresden.de (T. Gustmann).

1. Introduction

Shape memory alloys (SMAs) are outstanding materials, that can be utilized as actuators, couplings, sensors or high damping materials due to their reversible thermoelastic martensitic phase transformation [1,2]. Among them, binary NiTi, Cu-based and Fe-based alloys (furthermore: Co-based [3], Ti-Ta [4]) are the most attractive and well-studied SMA materials. Although NiTi alloys show an excellent biocompatibility and corrosion resistance with an outstanding shape memory effect and

superelasticity, these materials are normally expensive and challenging in terms of the manufacturing [5,6]. The disadvantage of Fe-based SMAs is that it is challenging to achieve reversible superelastic transformation at room temperature and pronounced degradation occurs in the shape memory properties under cyclic loading [7,8]. On the other hand, there is still an ongoing interest in Cu-based SMAs owing to their low cost, pronounced thermal conductivity, good processability as well as the promising shape memory properties and high damping capacity [9,10].

In the past decade, additive manufacturing (AM) has attracted considerable attention for producing SMAs. AM is a key technology and is expected to revolutionize the production of alloys and metals [1]. Laser powder bed fusion, also referred to as selective laser melting (SLM), is one of the most common and already industrialized AM processes in which each layer is created by local melting of a thin powder layer. By adjusting the parameters during the manufacturing process, microstructural features (e.g. phase formation, texture) can be controlled [11]. For instance, the energy dissipated in the material during melting dictates the change in grain morphology and size [12]. Since transformation temperatures (TTs) of SMAs are directly correlated with microstructural properties, SLM can be considered a powerful tool to tune the TTs of near-net-shaped parts, which are among the crucial criteria for a given application [13]. Another advantage of the SLM method, especially for Cu-based shape memory alloys [14], is its high intrinsic cooling rate of the order of 10^4 – 10^6 K/s [15] resulting from melting small volumes on massive substrate plates which leads to a suppression of the precipitation of brittle phases. This, however, always depends on the exact chemical composition of the applied material [14]. In general, precipitation hardening during processing can occur if *minor* additions of additional elements are present and/or might form with respect to the parameters used. The layer-by-layer fabrication constitute a repetitive heat input [16] which triggers (in situ heat treatment [17]) local phase formation or microsegregations [15].

The fabrication of Cu-based SMAs via SLM has been addressed in the literature. These studies focus on the processing of Cu-Al-Ni-Mn (Zr) [14,18–21], Cu-Al-Ni-Ti [22] and Cu-Zn-Al SMAs [23]. While the investigations on Cu-Al-Ni-Mn alloys mainly discuss the influence of process parameters and a remelting step on the transformation behavior for developing robust high-temperature Cu-based SMAs, Tian et al. [22] have linked the process optimization to the tensile properties of Cu-Al-Ni-Ti alloys. Preferential evaporation of Zn and the resulting difficulties in controlling the chemical composition in Cu-Zn-Al SMAs have been identified as a challenge [23]. In contrast to the listed studies, SLM of Cu-Al-Mn SMAs, which were proven to possess superior superelasticity [24,25], have not been investigated so far.

Kainuma et al. [26,27] have found that Cu-Al-Mn SMAs, containing about 17 at.% Al, show excellent ductility and good shape memory properties because of the low degree of ordering in the L2₁ parent phase. However, in order to achieve a large superelasticity, these alloys should possess adjusted microstructures as bamboo-like-grained, oligocrystalline or columnar-grained rather than having ordinary polycrystalline microstructures which are susceptible to intergranular cracking (strong elastic anisotropy) [28–36]. SLM is known for producing specimens with columnar grains, since solidification and partial remelting occurs towards the heat flow [37]. This enables the opportunity to produce Cu-Al-Mn SMAs with a high superelasticity by SLM due to providing improvement in the deformation compatibility and decreasing the stress concentration around grain boundaries [34].

Thanks to possessing high superelastic strains, Cu-Al-Mn SMAs are promising materials for different applications such as damping or solid-state refrigeration [38–40]. At this point, the SLM process provides an almost unlimited degree of freedom in terms of part geometry and allows the fabrication of complex components or spare parts for these applications. In addition, manufacturing delicate, topologically optimized lattice structures made of Cu-Al-Mn SMAs, which are known for their inherently high-damping capacity [41], could open the door for more efficient damping designs. Moreover, manufacturing of geometries with large surfaces and controlled open porosity (manipulation of the cooling performance) are not possible with conventional production techniques and it makes the SLM process especially attractive for novel elastocaloric cooling applications [42].

In this research, the processability of a Cu-Al-Mn SMA by SLM was examined for the first time. The effect of the processing parameters on the density and the TTs were systematically investigated. Moreover, the microstructure and corresponding shape memory properties were compared with induction cast material in order to better understand the behavior of samples produced by SLM.

2. Material and methods

2.1. Materials and processing

Gas-atomized powder of Cu_{71.6}Al₁₇Mn_{11.4} (at.%) with particle sizes smaller 75 μm (see Fig. 1(a) and (b)) was used in this work. This composition has been chosen because it has been proven to have excellent superelastic properties as a result of special thermo-mechanical heat treatments [29,30]. The pre-alloy was produced at Leibniz IFW Dresden in an induction furnace (Balzers) under argon atmosphere using high-purity elements (>99.9 wt%). Five cast rods with a diameter of 50 mm

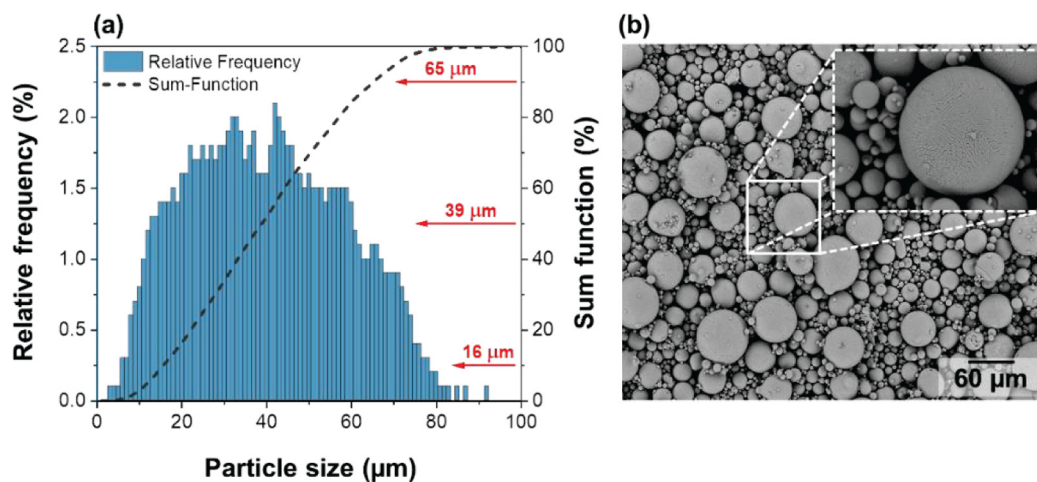


Fig. 1. (a) Particle size distribution analysis of the powder in as-sieved state. The particle size corresponds to the width of the particles. The highlighted numbers in red represent the d_{10} , d_{50} and d_{90} values. (b) A selected SEM image with an inset shows the size and shape of the particles.

and a length of 180 mm were prepared, cleaned and shipped to TLS Technik GmbH & Co Spezialpulver KG for the crucible-free atomization process (ELGA, argon atmosphere). The leftover of the atomization (approximately 50 mm in length) was used as a counterpart (extracted rods via electrical discharge machining: 3 to 5 mm diameter) for comparing the specimens fabricated via selective laser melting (SLM). Please note, all additively manufactured samples in this work are referred to SLM specimens (instead of PBF-LB). The prepared as-cast rods were solutionized at 900 °C for 3 h followed by water quenching and subsequently aged at 200 °C for 60 min (heat-treated state). These samples are designated as cast-HT. The aforementioned heat treatment sequence was also applied to a selected SLM sample to better understand the influence of the heat treatment on the properties of the differently manufactured samples.

All SLM samples (e.g. rods with separated contour rings: 7 mm diameter, 11 mm height) were fabricated under argon atmosphere in a SLM250^{HL} (400 W fiber laser, SLM Solutions Group AG). A laser beam focal offset of 2 mm has been used to compensate thermal drifts of the optics in order to apply a fine spot size of around 90 μm during processing. The layer thickness was adjusted to 50 μm and the scanning vectors (stripe hatching) between two subsequent layers were rotated mainly by 79° as this value is also used for conventional available materials for the SLM250^{HL} like AlSi10Mg or CuNi2SiCr. In addition, the point distance and exposure time regarding the scan vectors were held constant at 1 μm and 1 μs, respectively [14,19]. In order to establish a process window for the ternary alloy, process parameters like laser power (P : 200 to 350 W), scanning speed (v : 500 to 2000 mm/s) and the hatching distance (h : 0.09 to 0.15 mm) were systematically varied over a minimum of six different build jobs.

Every build job was analyzed by optical microscopy using a Keyence VHX-6000. Beside the track width of the contour rings (four measurements in total, see Fig. 2(b)) and surface appearance of the samples, selected cross-sections of the bulk samples were analyzed in terms of porosity. This information was then used to further fine-tune the parameters of already dense samples.

All SLM samples were aged at 200 °C for 30 min prior to the XRD and DSC measurements as well as the mechanical tests in order to stabilize the TTs. This has been also applied to Cu-Al-Mn SMAs in other studies [43–45].

2.2. Sample characterization

The gas-atomized powder was analyzed in terms of the particle size distribution and the particle morphology using a CamsizerX2 with an X-Jet module from Microtrac Retsch. For obtaining a solid statistical result for the powder batch, about 8 million of particles, viz. several grams of powder, were measured.

The chemical compositions of the cast and powder material as well as selected SLM specimens were determined using ICP-OES (Inductively Coupled Plasma Optical Emission Spectroscopy, device: iCAP 6500 Duo View, Thermo Fisher Scientific). Chemical point analysis from the cast sample was performed by (energy-dispersive X-ray spectroscopy; device: Xflash4010, Bruker) connected to SEM (Scanning Electron Microscope, device: Leo 1530 Gemini, Zeiss). The carbon content of the ingot material and the oxygen content of the powder were analyzed (minimum of three measurements) by carrier gas hot extraction in reactive and helium atmosphere, respectively (EMIA 820 V, Horiba and ON-836 Analyze, LECO, respectively).

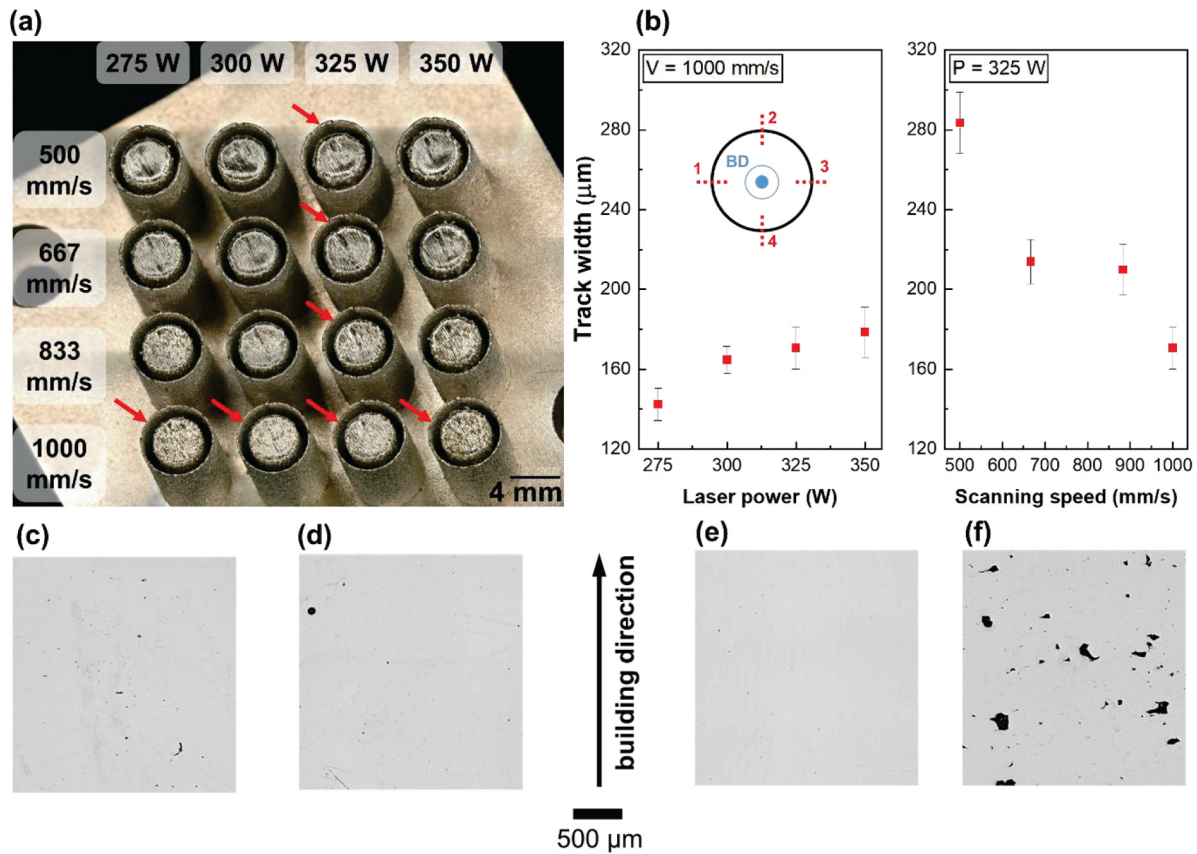


Fig. 2. (a) Overview of the first SLM build job using Cu-Al-Mn powder. The laser power (P , in W) and scanning speed (v , in mm/s) was varied as highlighted ($h = 0.1$ mm). To link the hatching distance with the approximate track overlap (cf. Table 1), separated contour rings were produced using the same P and v values as applied to the fabrication of the bulk parts. The influence of the line energy input on the track width (mean value) by either increasing P ($v = \text{const}$) or decreasing v ($P = \text{const}$) is shown in (b). The schematic inset shows the positions where the track width was analyzed. Cross-sectional micrographs for the pore size analysis were prepared from the samples (c) P1, (d) V1, (e) SLM-Ref and (f) V6. Please see Table 1 for further comparison.

The density of the bulk specimens was obtained by the Archimedean method using a balance (Sartorius MSA 225S). Selected samples were prepared for image analysis (ImageJ®) focusing on the grey value differences between the pores and solid material of the investigated cross-sections. In addition, the pore sizes and distributions were investigated using an X-ray computed tomography (Phoenix nanotom, General Electric), referred to as CT. The resolution of the tomography was adjusted at 5.9 µm and the scans were performed using a copper filter (0.3 mm in thickness) for the reduction of artifacts. 720 projections with an increased timing of 1500 ms per image were recorded in total for each reconstruction. The volume analysis was performed using VG-Studio max 2.2 (Volume Graphics).

Manually ground samples with thickness of less than 100 µm were used for X-ray diffraction (XRD). The analysis was performed using a STOE STADI P diffractometer with Mo-K_{α1} radiation ($\lambda = 0.7093187 \text{ \AA}$) in transmission mode. The patterns were analyzed by X'Pert High-Score Plus software, and an ICSD PDF-2 plus database (ICSD, The Inorganic Crystal Structure Database, FIZ Karlsruhe).

For microstructural examinations, samples were cut, ground and polished in two steps with 3 and 1 µm, finally prepared with OP-S suspension (Struers). Some of the polished samples were etched in 10% Nital solution. Images were recorded using a digital confocal microscope (Keyence VHX-6000 and VHX-7000). The grain morphology and crystallographic orientations of additional vibration polished (OP-S, 4 h) SLM and cast samples were investigated in a scanning electron microscope (SEM, Zeiss Gemini Leo 1530) equipped with a Bruker e-Flash HR 1000 electron backscatter diffraction (EBSD) detector. Texture and grain size measurements (misorientation angle: 2–5°) were carried out using the software Esprit 2.2 (Bruker).

The TTs were determined by differential scanning calorimetry (DSC) in a Perkin-Elmer DSC 8500 at a heating and cooling rate of 10 °C/min. All samples were investigated by applying a minimum of two cycles (–80 to 100 °C). Cooling was achieved by using liquid nitrogen.

The cast material and selected SLM samples (please see Section 3.1 for further details) were used for mechanical testing at room temperature (Instron 5869, compression mode). Specimens with a diameter of 3 mm and height of 6 mm were used and the strain was measured with a laser extensometer (Fiedler Optoelektronik). Firstly, samples were loaded under monotonic loading until 40% strain. Secondly, incremental-strain experiments until 8% strain level were applied to determine the superelastic properties. After an initial loading to 1% strain, the samples were unloaded and then this protocol was maintained by increasing the applied strain by 1% at each step. Strain control at an initial rate of $5 \times 10^{-4} \text{ s}^{-1}$ was used during both loading and unloading. For mechanical testing, at least two samples of each condition were measured.

3. Results and discussion

The aim of the present study is to investigate the interrelations between the processing, the microstructure and the resulting shape memory behavior in case of an additively manufactured Cu_{71.6}Al₁₇Mn_{11.4} alloy. To the best of our knowledge, Cu-Al-Mn alloys have not been prepared by laser powder bed fusion so far. Hence, we will first address the systematic development of the process parameters in detail in Section 3.1. Sections 3.2 and 3.3 discuss the influence of the applied process parameters and the manufacturing technique itself (cast vs. SLM) on the resulting microstructures as well as the corresponding transformation temperatures. The question of how the microstructures affects the mechanical properties, especially the shape recovery, will be addressed in Section 3.4.

3.1. Powder analysis and optimization of process parameters

A key aspect for obtaining highly dense specimens via laser powder bed fusion, beside pronounced weldability of the alloy, whereby Cu-Al-Mn alloys are excellent in this regard [46,47], and an adjusted process

[48], is the suitability of the powder material for manufacturing [49]. In other words, the powder must be mostly spherical (high apparent density), free flowing (homogenous powder layers) and free of pores (hollow spheres). Thus, the size and shape of the gas-atomized powder has been characterized by means of dynamic picture analysis and SEM (Fig. 1).

In general, most powders for laser powder bed fusion are in the range of 15–63 µm to fulfill certain needs like appropriate flowability, low impurity contents, high apparent density and particle sizes smaller than the laser beam diameter to obtain homogenous melt tracks [19,49]. As we have decided to focus on the fabrication of bulk materials via using relatively high laser powers, we adjusted the particle size range above the aforementioned criteria. A further consequence was that almost 70% of the atomized material was efficiently used in this way (as-delivered non-sieved powder: 14.5 kg, as-sieved powder: 10 kg).

The PSD (particle size distribution: $d_{10} = 16 \text{ \mu m}$, $d_{50} = 39 \text{ \mu m}$, $d_{90} = 65 \text{ \mu m}$) fits well with the pre-defined particle size range (below 75 µm). This shows that the sieving procedure (ultrasonic sieving under argon) before processing can be carried out efficiently for small as-atomized batches. This approach was, furthermore, preferred to also eliminate residual moisture. Most particles have a size of around 40 µm (see also Fig. 1(a)). A slightly increased but uncritical amount of particles below 10 µm (3%) and above 75 µm (2%) were observed. Due to an anisotropy mean value (width-to-length ratio of the determined particles) of 0.925 and a pronounced symmetry (almost no satellites, see Fig. 1(b)) of the powder particles, an excellent flowability has been observed. This has been further tested via performing recoat trials in the SLM250^{HL} machine (not shown).

In order to determine a suitable process window for the fabrication of Cu-Al-Mn parts, several cylindrical specimens with a height of 11 mm were manufactured as shown in Fig. 2(a). For every rod, a contour exposure was added (outer diameter = 7 mm) to check the influence of the line energy input (described in detail in [19,50]) on the resulting contour/track width by simply using the same laser power and scanning speed applied for the rod (diameter = 5 mm). In general, the density of SLM samples is strongly affected by the volumetric energy input [51], which can be estimated as [21]:

$$E = \frac{P}{v \cdot h \cdot l} \quad (1)$$

with P : laser power, v : scanning speed, h : hatching distance and l : layer thickness. In the first step, we tried to establish the optimum values for the laser power ($P = 275$ to 350 W) and scanning speed ($v = 500$ to 1000 mm/s). Thus, the hatching distance was kept constant at 0.1 mm in the beginning. Please note, we have kept the laser power around 300 W as it is reported that complete melting for Cu-based shape memory alloys (layer thicknesses: 50 to 100 µm) is promoted at relative high laser powers [18,19]. Fig. 2(a) illustrates that samples with the shown parameters were successfully fabricated (no cracks, delamination). The resulting density values are close to each other (see Table 1). Since we found that no cast or SLM sample is free of pores, the density of the counterparts was evaluated by Archimedean measurements (in g/cm^3) without determining the relative density. Regarding the SLM samples, specimens with similar density values were visually checked (surface appearance: smoothness, roughness) and further characterized via cross-sectional analysis and CT (details see below).

In the investigated parameter window (selected SLM specimens are shown in Table 1), no obvious trend between the density and energy input, by systematically changing P (275 to 350 W, v and h : constant) or v (500 to 2000 mm/s, P and h : constant), was observed. It is noteworthy that when samples are processed with a track overlap of 35 to 45%, which corresponds to an energy input of around 60 J/mm^3 , the density is highest (7.32 g/cm^3) and the top surface of these specimens is smooth (cf. samples in Fig. 2(a)). These results are similar to the findings for Cu-Al-Ni-Mn shape memory alloys [14,19,21,52] and, thus, allow us to

Table 1

Summary of the process parameters (P : laser power, v : scanning speed, h : hatching distance, TO : track overlap, E : volumetric energy input) used for selected Cu-Al-Mn specimens. The samples shown were also used for further analysis (see Sections 3.2 to 3.4). SLM samples produced with 325 W laser power, 1000 mm/s scanning speed and 0.1 mm hatching distance are the so-called reference specimens (SLM-Ref). The letters (P1, V1, etc.) stand for SLM samples where just the implied process parameter was varied.

Sample	P (W)	v (mm/s)	h (mm)	Track overlap (%)	E (J/mm ³)	Density (g/cm ³)
Cast (ingot material)	–					7.30 ± 0.01
P1	275	1000	0.1	30	55	7.30 ± 0.01
P2	300	1000	0.1	40	60	7.32 ± 0.02
V1	325	500	0.1	65	130	7.30 ± 0.01
V2	325	667	0.1	55	97.5	7.31 ± 0.01
V3	325	833	0.1	50	78	7.31 ± 0.01
SLM-Ref	325	1000	0.1	40	65	7.32 ± 0.01
V5	325	1500	0.1	–	43.3	7.30 ± 0.01
V6	325	2000	0.1	–	32.5	7.18 ± 0.02
H1	325	1000	0.09	45	72.2	7.31 ± 0.01
H3	325	1000	0.11	35	59.1	7.32 ± 0.02
H4	325	1000	0.12	30	54.2	7.31 ± 0.01
P4	350	1000	0.1	45	70	7.32 ± 0.01

summarize that controlling the track overlap for a certain combination of laser power and scanning speed is a useful tool to speed up the process optimization. Furthermore, producing separated contour rings enables us to investigate the side surface roughness and find promising parameter combinations for the manufacturing of relatively smooth parts as the outer contour of these components is usually clad by a single or double boundary scan [53].

Based on the parameter variations used and the comparison of all density values for a number of six build jobs, the SLM samples fabricated with $P = 325$ W, $v = 1000$ mm/s and a hatching distance of 0.1 mm ($E = 65$ J/mm³, $\rho = 7.32 \pm 0.01$ g/cm³) were determined as the reference samples. While the density observed was among the highest (see

also Fig. 2(e), porosity = 0.10%), the surface appearance (sides, top surface) was determined to be one of the smoothest of all produced parts.

In addition to the density measurement via the Archimedean method, a number of four SLM specimens (P1, V1, SLM-Ref and V6) were selected for a further investigation of the residual porosity (see Fig. 2(c) to (f)). While V1 is produced with the maximum energy input ($E = 130$ J/mm³), the minimum energy ($E = 32.5$ J/mm³) was used for the fabrication of sample V6. This sample, in particular, was processed with a much higher scanning speed than other candidates to see when the density drops significantly due to lack of fusion [11] effects (see Fig. 2(f), porosity = 2.90%). The same procedure has been repeated regarding the laser power ($P_{\min} = 200$ W), which resulted in a similar finding (not shown). While Fig. 2(c) shows that some irregular pores are present (sample P1, porosity = 0.37%), only a few small spherical pores are observed in sample V1 (see Fig. 2(d), porosity = 0.25%). Interestingly, the density shows a much higher sensitivity to the laser power (50 W difference to SLM-Ref) as to the scanning speed (500 mm/s difference to SLM-Ref). This can be explained by the fact that Cu and Cu alloys generally require a relative high laser power when processed with an infrared laser [54].

According to our detailed investigation on the optimization of process parameters for Cu_{71.6}Al₁₇Mn_{11.4}, the evaluated parameters (SLM-Ref, see Table 1) were transferred to the manufacturing of individually designed structures (Fig. 3(a)). All produced samples, irrespective of the sample size or complexity, revealed smooth surfaces and no defects. This proves that individually designed, high-quality components can be produced via laser powder bed fusion. The lattice structure and the tension spring were successfully built up on block supports using a line energy input of 0.275 J/mm ($P = 275$ W, $v = 1000$ mm/s) and a more focused laser beam in contrast to the bulk specimens. For a further comparison of the sample quality, the highlighted sample in Fig. 3(a) has been removed and investigated via CT (Fig. 3(b)). Even if a few pores are present, the porosity ($0.1 \pm 0.04\%$) is very low and comparable to the cast state ($0.1 \pm 0.05\%$) which was found to be in the same density region for this particular case (Fig. 3(d)). A very high density was also obtained by SLM processing with a slightly different scanning strategy (vector rotation from layer to layer = 90°, Fig. 3(c)). A change in the vector rotation is a common technique to further adjust the quality [14] and especially to change the materials properties [48].

3.2. Chemical and microstructural analysis

The chemical compositions of the cast ingot, atomized powder and SLM-Ref sample are listed in Table 2. Please note that five different

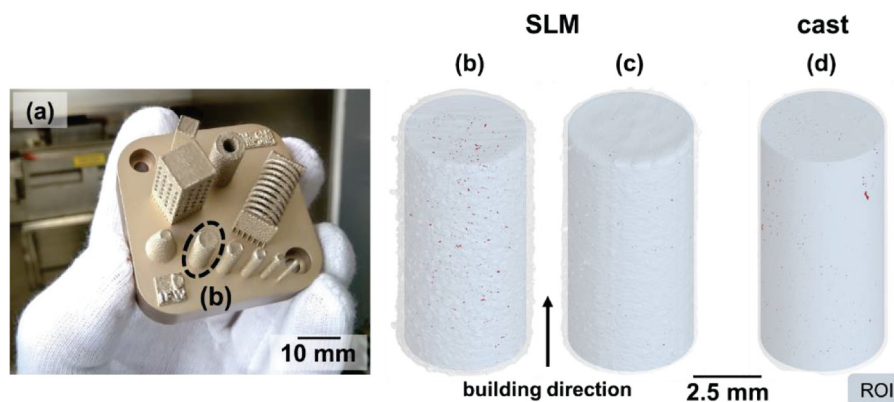


Fig. 3. (a) Image of a set of rods, beams and more complex geometries (hollow cylinder, lattice structure, prototypical tension spring) produced by using optimized parameters (SLM-Ref, $P = 325$ W, $v = 1000$ mm/s, $h = 0.1$ mm). (b) The marked sample (diameter = 5 mm, height = 11 mm) was removed for a detailed 3D analysis via X-ray computed tomography. The other reconstructed, transparent CT-images are representatives of a (c) SLM-Ref rod with a slightly changed scanning rotation (90°) and (d) cast specimen. The investigated area regarding the porosity (region of interest - ROI) is highlighted (pores: red, (b) porosity = $0.1 \pm 0.04\%$, (c) porosity < 0.01%, (d) porosity = $0.1 \pm 0.05\%$).

Table 2

Nominal and experimental determined chemical compositions of the cast material, the powder as well as selected SLM samples. SLM* and SLM** samples were not shown in Table 1 and were only used for ICP-OES measurements.

					Cu (at.%)	Al (at.%)	Mn (at.%)
Nominal composition					71.6	17	11.4
As-cast ingot					71.28 ± 0.24	17.51 ± 0.12	11.21 ± 0.10
Powder material					71.88 ± 0.32	16.87 ± 0.06	11.25 ± 0.06
Sample	P (W)	v (mm/s)	h (mm)	E (J/mm ³)			
V1	325	500	0.10	130.0	72.02 ± 0.32	16.91 ± 0.20	11.07 ± 0.08
SLM*	275	667	0.10	82.5	72.07 ± 0.34	16.91 ± 0.06	11.02 ± 0.06
P4	350	1000	0.10	70.0	72.10 ± 0.70	16.95 ± 0.08	10.94 ± 0.16
SLM-Ref	325	1000	0.10	65.0	72.00 ± 0.38	16.87 ± 0.10	11.13 ± 0.08
SLM**	300	1000	0.11	54.6	72.02 ± 0.63	16.87 ± 0.06	11.10 ± 0.08

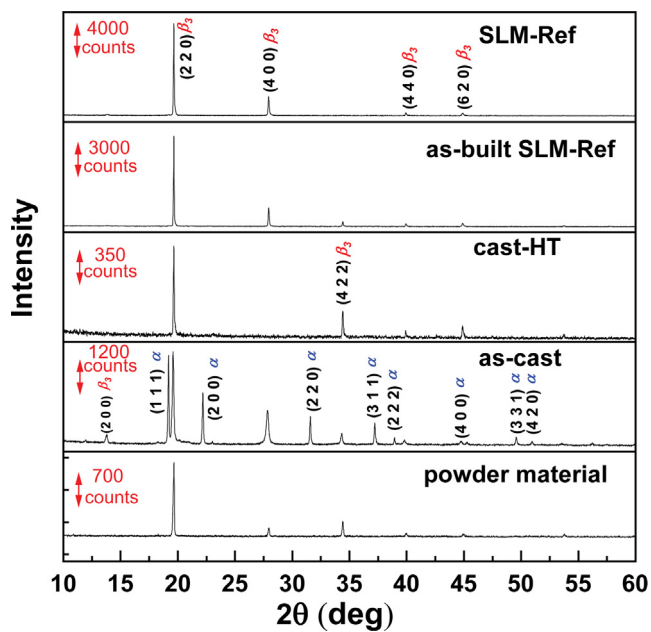


Fig. 4. XRD patterns of the powder, as-cast, cast-HT, as-built SLM-Ref (without low-temperature aging) and SLM-Ref (with 200 °C 30 min aging) samples.

ingots with a nominal composition of $\text{Cu}_{71.6}\text{Al}_{17}\text{Mn}_{11.4}$ (at.%) were produced for our approach. Two of them were analyzed by means of ICP-OES and it has been observed that there is a 1.7% difference in the Al content (in Table 2, only the results for the investigated ingot (XRD, EBSD, DSC, etc.) are shown). However, the composition of the powder which is atomized from five produced ingots is very close to the nominal composition.

Irrespective of the energy input, the composition of the SLM samples is identical within the experimental error (cf. Table 2). Only small deviations in the Mn content (experimental error of the measurement method) imply that manufacturing via SLM does not cause composition changes in the $\text{Cu}_{71.6}\text{Al}_{17}\text{Mn}_{11.4}$ alloy, in contrast to NiTi [55,56] and Cu-Zn-Al [23] SMAs alloys that suffer from preferential evaporation of Ni and Zn, respectively. It should be also noted that the carbon content of the cast ingot and oxygen content of the powder were measured as 0.006 ± 0.0006 and 0.011 ± 0.0002 wt%, respectively, which shows the low impurity level of the in-house processed alloy and further matches with our findings for Cu-Al-Ni-Mn [14,19,21].

Fig. 4 shows the XRD patterns of the powder, as-cast, cast-HT and SLM-Ref (with and without 200 °C 30 min aging) specimens. The results illustrate that all specimens except the as-cast condition contain only parent phase (austenite) with a $L2_1$ structure. Low-temperature aging did not cause a change regarding the austenite. It is applied for

Cu-Al-Mn alloys to stabilize the forward and reverse transformation [57,58].

The as-cast sample contains a Cu-rich face-centered cubic phase (α : Fm $\bar{3}m$ space group) in addition to the austenite due to the relatively low cooling rate during processing. It is known that α phase precipitates in Cu-Al-Mn alloys, containing approximately 17 at.% Al, form when relative slow cooling rates are present [6]. The α phase precipitates in the as-cast material have a high volume fraction as shown in Fig. 5(a). EDX point analysis shown in Fig. S1 revealed that Cu-rich α precipitates caused a composition change in the matrix by decreasing Cu and increasing Al content. In addition, the formation of α phase suppresses the martensitic transformation due to the decrease in the mobility of the martensite/austenite interfaces [59]. Therefore, cast samples did not show any martensitic transformation (not shown in this work). This is the reason why cast samples had to be solution-treated for obtaining superelasticity at room temperature (see Sections 3.3 and 3.4).

Microstructures of the as-cast, cast-HT, SLM-Ref and SLM-Ref-HT (as-built +900 °C 3 h + 200 °C 60 min) specimens were examined by optical microscopy as seen in Fig. 5. The α phase is clearly seen in the as-cast sample in agreement with the XRD analysis. Coarse grains, most of which are in the range of millimeters, were obtained by applying a 3 h solution treatment at 900 °C to the as-cast sample (see Fig. 5 (b)). The microstructure of the SLM-Ref sample consists of elongated columnar grains oriented in the building direction (Fig. 5(c)) due to the partial re-melting of the underlying solid material and epitaxial grain growth in the direction of heat transfer towards the base plate [60,61]. The 3 h solutionizing step applied to a SLM-Ref sample causes an obviously grain coarsening as depicted in Fig. 5(d)). The grains formed were partially as big as grains measured in the cast-HT specimen.

Fig. 6 shows the microstructures of the cast-HT and SLM-Ref samples, which were analyzed by means of EBSD. Only austenite ($L2_1$) was detected in both samples, which confirms our findings via XRD (cf. Fig. 4). As the investigated area contains relatively few grains with random orientation, an anisotropic microstructure was observed in an area of 2.8 mm × 2 mm (Fig. 6(c) and (f)).

In contrast to the cast material, the microstructure of the SLM-Ref sample shows columnar grains with a pronounced length-to-width ratio together with some fine subgrains (Fig. 6(b)) aligned in the building direction (BD). The grains have a strong [001]-texture along the BD. This is similar to the results for continuous-cast specimens, which exhibit a pronounced superelasticity above 10% shape recovery [34–36]. A strong [001]-texture along the BD has been obtained by different research groups for numerous alloys (cubic lattice structure) produced by laser powder bed fusion [62–65]. Therefore, SLM processing of Cu-Al-Mn seems a viable path for producing shape memory parts with high superelasticity at room temperature. The next important step to promote superelasticity in additively manufactured samples would be to further increase the width of the columnar grains in order to reduce the grain constraints. Regarding the discussed assumption, a proper

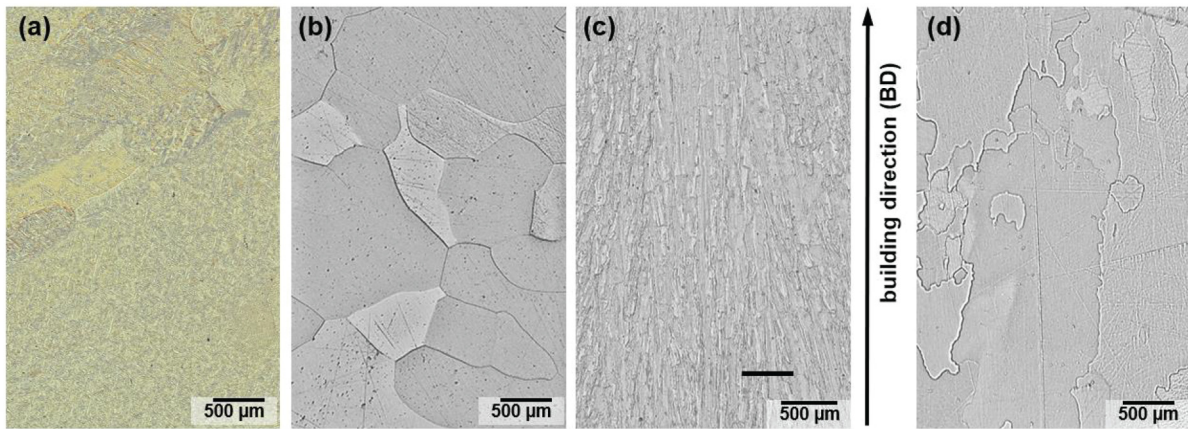


Fig. 5. Optical microscopy images of (a) as-cast, (b) cast-HT, (c) SLM-Ref and (d) SLM-Ref-HT (as-built + 900 °C 3 h + 200 °C 60 min) samples. Images (c) and (d) are showing the microstructure of the samples in building direction.

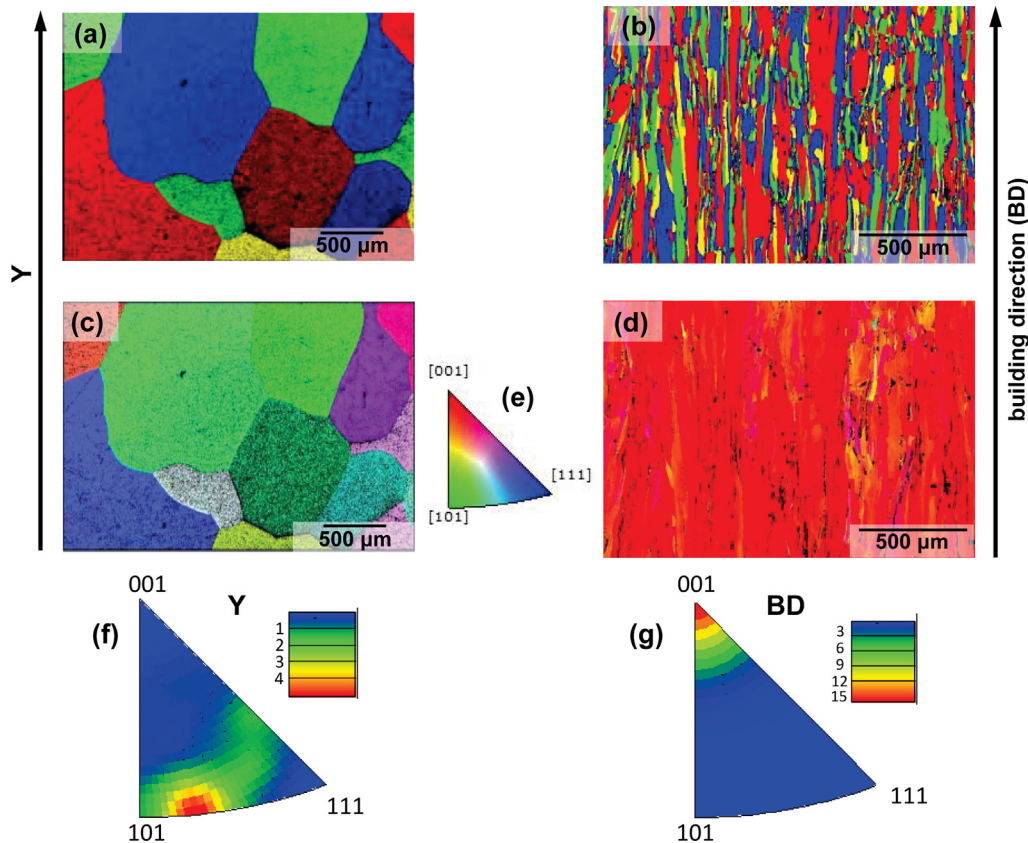


Fig. 6. EBSD maps showing the microstructure along the (a, c, f) Y direction of the cast-HT and (b, d, g) building direction (BD) of SLM-Ref samples. The overview shows in detail the (a, b) grain map of the austenite, (c, d) colour-coded grains in terms of the texture (see also (e)) and the (f, g) inverse pole figures (IPFs). The image in the middle (e) represents the IPF coloring scheme for (c) and (d).

scanning strategy [21] and/or an adjusted heat treatment (abnormal grain growth [64]) should be carried out.

3.3. Transformation temperatures

The transformation temperatures (TTs) of $\text{Cu}_{71.6}\text{Al}_{17}\text{Mn}_{11.4}$ produced by induction melting (cast) and SLM were measured, and the resulting DSC curves from the second cycles are shown in Fig. 7. Forward and reverse peak temperatures (M_p and A_p), reverse

transformation intervals (A_f-A_s) and transformation hysteresis (A_f-M_s) were calculated from the second cycles of DSC results and are shown in Table 3.

The jerky characteristic of the DSC peaks during transformation, as seen for the solutionized samples, can be attributed to the slight variations in transformation characteristics of different regions of the coarse-grained samples [66]. This multiple-peak behavior is also observed in Ni-Mn-Ga and Fe-Mn-Ga based martensitic Heusler alloys due to the sudden progress of large austenite/martensite phase

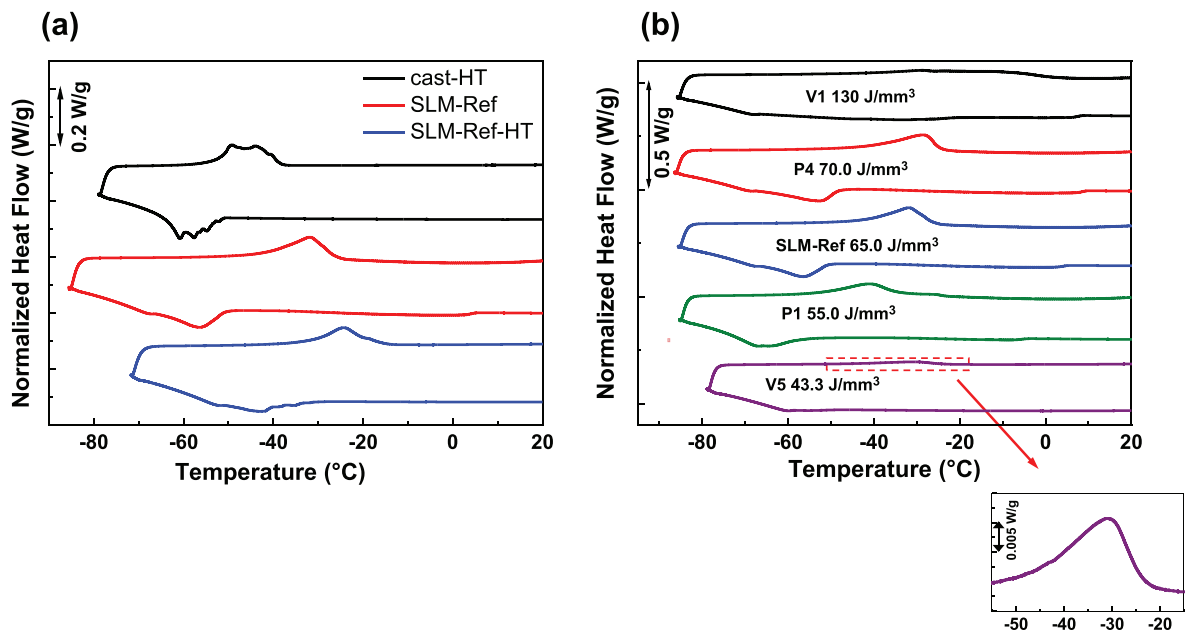


Fig. 7. Second DSC cycles of (a) cast-HT, SLM-Ref and SLM-Ref-HT samples. The curves in (b) show the transformation behavior when SLM samples, produced with different energy inputs (heat treatment as SLM-Ref), are heated (martensite to austenite) and cooled (austenite to martensite).

Table 3

Comparison of the transformation temperatures (TTs) (M_p : peak value austenite-to-martensite, A_p : peak value martensite-to-austenite transformation, A_f-A_s : peak width backward transformation, A_f-M_s : thermal hysteresis) for the cast-HT and SLM samples produced with different energy inputs.

Sample	E (J/mm ³)	M_p (°C)	A_p (°C)	A_f-A_s (°C)	Thermal hysteresis (A_f-M_s) (°C)
cast-HT	–	≈ – 58	≈ – 47	145	14
P1	55	–67	–41	19	23
P2	60	–60	–35	17	24
V1	130	No clear transformation			
V2	97.5	–47	–25	35	27
V3	78	–54	–30	31	25
SLM-Ref	65	–56	–32	16	25
SLM-Ref-HT	65	–43	–24	15	16
V5	43.3	No clear transformation			
V6	32.5				
H1	72.2	–54	–29	18	24
H3	59.1	–59	–34	15	26
H4	54.2	–62	–37	14	24
P4	70	–53	–29	17	26

boundaries [67,68]. Moreover, DSC samples typically consist of only few grains with random orientation and this causes them to behave differently from the polycrystalline structures. While the martensitic transformation begins at different temperatures within the grains, it also finishes at different temperatures which leads to appear in a multi-step transformation [69].

Considering that the grain sizes of the solutionized cast and SLM-Ref material are close to each other, the differences in TTs between these samples have to be attributed to their slightly shifted Al contents [70,71]. Thus, lower TTs of the cast-HT sample can be directly linked with the higher Al content of the cast material (approximately 0.6% difference in Al content, see Table 2). While the SLM-Ref material is composed of columnar grains with a size of tens of micrometers, solutionized specimens consist of large grains of the order of millimeters. This huge increase in the grain size leads to a decrease in the grain constraints, which facilitates the nucleation of martensite [72]. Therefore, TTs increase with the shift of the grain size towards larger

values [73]. Although the transformation interval (A_f-A_s) of the samples is close to each other, temperature hysteresis (A_f-M_s) of the SLM-Ref sample is about 10 °C larger than for the samples in the solutionized states. A larger thermal hysteresis is attributed to the large number of grains and grain boundaries, since dissipative energy increases when more martensite interfaces near the grain boundaries are present [74].

In addition to the aforementioned results, curves from the second DSC cycle of selected SLM samples, fabricated with different process parameters, are shown in Fig. 7(b). Although sample V5 has a relatively high density (7.30 ± 0.01 g/cm³) and is a promising candidate regarding the sample quality, it only shows a weak transformation with a very small transformation enthalpy as highlighted in the inset. Likewise, sample V1 exhibited a similar martensitic transformation behavior, but at higher temperatures compared to sample V5. Such a broadening and disappearing of the peaks could be an indication for an inhomogeneous transformation [51,75]. In XRD measurements (which are not shown here), very small additional reflections were found for the samples produced with 40 and 140 J/mm³. Therefore, formation of a secondary phase might have caused inhomogeneities and concentration differences among the samples which trigger the flattening of the transformation peaks. This has to be addressed more in detail by further microstructural investigations and is out of the scope of the work shown here.

The DSC traces of the different SLM samples reveal that the TTs (e.g. M_p , A_p) can be controlled during laser powder bed fusion. Please note that the transformation temperatures of the forward transformation follow the trend of the temperatures discussed more in detail (reverse transformation) and we will therefore slightly shorten our discussion at this point. The aforementioned temperatures as well as A_f-A_s and A_f-M_s values of all the investigated SLM specimens, as a function of the energy input (E), are plotted in Fig. 8(a) and (b). While no significant change is observed in the thermal hysteresis (A_f-M_s), the transformation range (A_f-A_s) tends to increase with higher energy inputs. A significant increase is seen in samples V3 and V2 (cf. Table 1) produced with relatively low scanning speeds (833.3 and 666.7 mm/s, respectively). The reasons for the broadening of the transformation peak are associated with the increase in heterogeneity of the microstructures as stated above.

Table 3 and Fig. 8 reveal that M_p and A_p temperatures are shifting towards larger values when the energy input increases. Similar findings

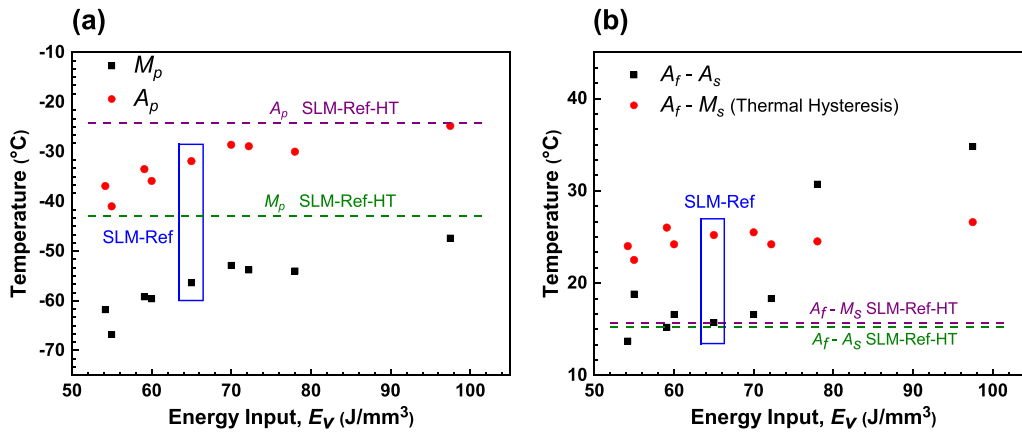


Fig. 8. The change of (a) M_p, A_p temperatures and (b) $A_f - A_s$ (transformation peak width) as well as $A_f - M_s$ (thermal hysteresis) values as a function of applied energy input. The values of the SLM-Ref-HT sample were added to the plots for comparison.

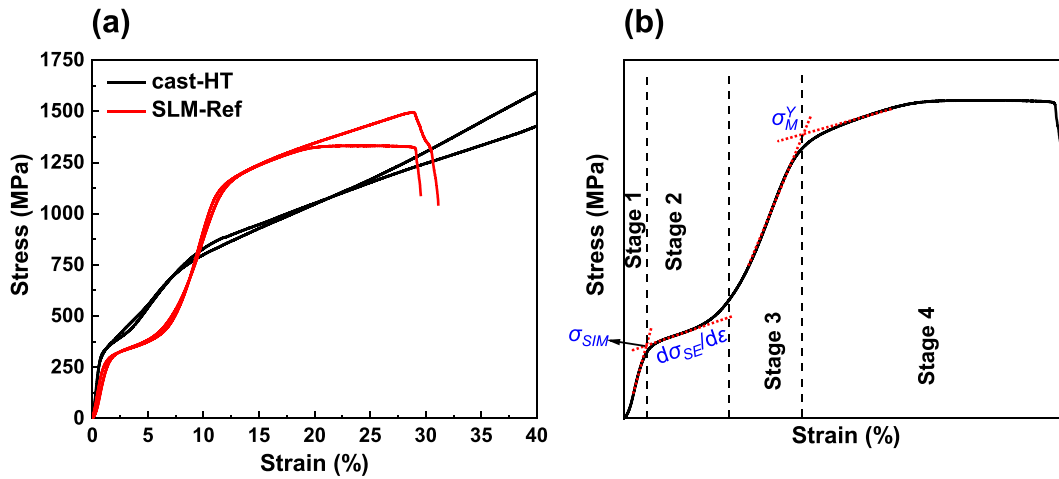


Fig. 9. (a) Compressive stress-strain curves of the cast-HT and the SLM-Ref samples obtained at room temperature (test was stopped at 40% strain level for cast-HT samples). (b) Illustration of how critical stress of SIMT (σ_{SIM}), the slope of SIMT ($d\sigma_{SE}/d\epsilon$) and the yield strength of the martensite (σ_M^Y) were determined (Stage 1: elastic deformation of the austenite, Stage 2: stress-induced martensitic transformation, Stage 3: elastic deformation of the martensite, Stage 4: plastic deformation of the martensite).

are reported in several studies related to additively manufactured Cu-based [21] and, especially, NiTi SMAs [51,55,76,77]. Pronounced evaporation of Ni with an increasing energy input was found to be the dominant factor for the alteration of TTs of NiTi alloys. The factor of chemical composition differences among the SLM samples can be excluded for our study according to the ICP-OES measurements we have discussed earlier. As tabulated in Table 2, the chemical composition results are quite close to each other irrespective of the applied energy input.

Grain size and grain morphology [78,79], defect density [9,80] and degree of order [6,26,27] are other general factors affecting the TTs of Cu-based SMAs along with their chemical composition. The SLM process parameters can be varied to control the cooling rate and melt pool morphology [62] and thus, the energy input with respect to the applied parameters. In other words, the energy input plays a dominant role regarding the grain size evolution [12]. Please note that it is very challenging to correlate microstructural aspects (e.g. grain size) and TTs especially for those samples, which have been additively manufactured [19,21]. Beside the thermal history, which is specific to each combination of process parameters and the corresponding scanning pattern [48,62], the degree of order of the parent phase and defect concentration change substantially owing to differences in the cooling rates are

other governing factors [14,81]. Therefore, a comprehensive study on the relationship between the TTs and processing parameters has to be performed. However, the above results indicate that a systematic change of the energy input in defined limits results in adjustable TTs as it has been also observed for Cu-Al-Ni-Mn [21,52] and Cu-Al-Ni-Mn-Zr [14]. In other words, laser powder bed fusion can serve as an efficient fabrication tool to obtain Cu-Al-Mn parts with (locally) adjusted TTs without the need for any compositional change or further heat treatment steps.

3.4. Mechanical properties

Final experiments were done to evaluate the mechanical and superelastic behavior of the SLM-Ref sample by comparing the results with those of cast-HT samples. Loading direction of the SLM-Ref samples was parallel to the building direction in all the tests. Fig. 9(a) presents the compressive stress-strain curves for the cast-HT and SLM-Ref samples under quasi-static loading at room temperature. Two samples of each condition were tested in order to investigate the stress-induced martensitic transformation and to assess the yield strength of the martensite. Critical stress values of SIMT (σ_{SIM}), the slope of SIMT ($d\sigma_{SE}/d\epsilon$) and the yield strength of the detwinned martensite (σ_M^Y)

Table 4

Mechanical data determined from Fig. 9(a) and Fig. 10(a). The elongation and σ_M^Y values were determined from Fig. 9(a). Shape recovery rates were calculated based on the curves shown in Fig. 10(a). σ_{SIM} and $d\sigma_{SE}/d\varepsilon$ values were calculated from both Fig. 9(a) and Fig. 10(a). Please note that the compression strength and elongation values of the cast-HT sample were not added since the test has been stopped manually after initial macroscopic crack initiation.

Sample	Critical stress of stress-induced martensitic transformation (σ_{SIM}) (MPa)	Slope of stress-induced martensitic transformation ($d\sigma_{SE}/d\varepsilon$) (GPa)	Yield stress of martensite (σ_M^Y)	Shape recovery (%)	
				2% deformation	4% deformation
cast-HT	370 ± 49	4.98 ± 0.50	790 ± 45	80.0 ± 1.9	59.7 ± 1.9
SLM-Ref	302 ± 4	2.04 ± 0.12	1158 ± 3	80.7 ± 0.8	65.3 ± 2.5

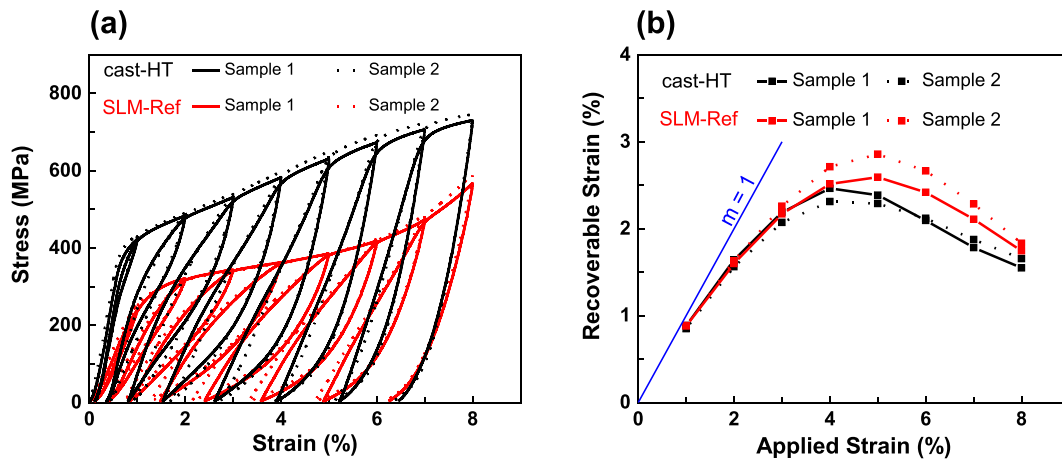


Fig. 10. Compressive superelastic responses of the cast-HT and the SLM-Ref specimens under incremental strain testing at room temperature (a). The recoverable strain values were extracted from (a) and plotted as a function of the applied strain (b). The solid line is a guide for the eye indicating full strain recovery.

(for the determination of these values, please refer to Fig. 9(b)), as well as ultimate compression strength and the elongation values are listed in Table 4. The values obtained from superelastic testing (Fig. 10(a)) were also taken into account to calculate the mean values of σ_{SIM} and $d\sigma_{SE}/d\varepsilon$. Large deviations observed in the results of the cast-HT sample could be attributed to an anisotropic microstructure specific to each sample (grains can span over the whole cross-section) (see Fig. 5(b) and Fig. 6(a)).

SLM-Ref sample has much lower $d\sigma_{SE}/d\varepsilon$ value compared to cast-HT sample (please see Table 4). This value indicates the work-hardening rate of superelastic deformation and a higher $d\sigma_{SE}/d\varepsilon$ is directly associated with the increase in slip defects [36,73]. Therefore, superelastic strain is affected adversely as $d\sigma_{SE}/d\varepsilon$ increases. It can be seen that the refined microstructure of the SLM-Ref sample leads to higher σ_M^Y values, which implies the high resistance against dislocation slip of this sample compared to the cast-HT counterpart. As a result of strength-ductility tradeoff, cast-HT sample possesses a higher ductility or, in other words, this result highlights that also coarse-grained Cu-Al-Mn can show large deformations.

The superelastic behavior of the samples manufactured via casting and SLM was compared using incremental loading-unloading experiments. Stress-strain curves of two samples from each condition are shown in Fig. 10(a) and the recoverable strain values as a function of the applied strain are compared in Fig. 10(b). The SLM-Ref samples exhibited a higher shape recovery compared to its conventional counterpart. The maximum recoverable strains were obtained as 2.86 and 2.59% in case of an applied strain of around 5%. On the other hand, the maximum values are 2.46 and 2.31% after 4% strain for cast-HT sample 1 and 2, respectively. While both conditions imply that about 80% average shape recovery at 2% applied strain is achievable, the SLM-Ref sample showed about 65% shape recovery which is about 5% more than that

of cast-HT sample under 4% deformation (cf. Table 4). Consequently, samples prepared by laser powder bed fusion have a superior mechanical and superelastic performance at room temperature compared to its cast counterparts due to the fine-grained and favorably textured microstructure. In addition, SLM samples exhibited repeatable results, contrary to what was found for the cast specimens.

It is known that ordinary polycrystalline Cu-based SMAs have only a limited recoverable strain as we observed in the cast-HT sample due to the high elastic anisotropy and an associating local plastic deformations at grain boundaries [28,34,58]. Although SLM-Ref samples have high σ_M^Y values, which generally suppresses irreversible deformation by slip, the increase in the grain constraint due to its small grain size is thought to be a hampering factor for not obtaining an excellent superelastic performance as it is reported for bamboo-like-grained, oligocrystalline [24,25] or columnar-grained structures [34–36].

4. Conclusions

In this study, a superelastic Cu-Al-Mn shape memory alloy was manufactured by laser powder bed fusion. The effect of the process parameters on the relative density and transformation behavior was investigated. Microstructural and mechanical properties of selected additively manufactured samples were compared with those of conventionally cast samples. The main findings are outlined as follows:

1. Crack-free samples with a similar density were successfully produced across a wide range of energy inputs (43.3 to 130 J/mm³). A change in the chemical composition depending on the energy input was not observed.
2. Unlike the cast material, fully austenitic SLM samples were obtained due to rapid cooling after melting. Thus, a solutionizing heat

treatment step which is used to dissolve the α precipitates (as-cast ingot material) and promote the shape memory properties is not needed for the additively manufactured samples.

- The transformation temperatures of additively processed bulk samples shifted towards higher values as the energy input were increased. Therefore, this manufacturing method can offer an efficient approach for tailoring the transformation temperatures of Cu-Al-Mn alloys through carefully selecting the process parameters. This is even more important due to the fact that the martensitic transformation degrades if, irrespective of the energy input, one process parameter is changed drastically, viz. by a factor of two, with respect to the reference parameter setup.
- Columnar grains with a strong [001]-texture along the building direction were formed in the additively fabricated material. The additively fabricated samples have shown higher yield stresses and superelastic strains compared to the cast sample.

To sum up, we have demonstrated that laser powder bed fusion is a suitable tool to manufacture individually designed superelastic Cu-Al-Mn parts and there is a great potential for producing samples with a high superelasticity once the microstructure in terms of the grain size and distribution can be further controlled (bamboo-grained or directional solidified microstructures).

Supplementary data to this article can be found online at <https://doi.org/10.1016/j.matdes.2021.109625>.

Availability of data and material

The data supporting the findings of this study are available from the corresponding authors on reasonable request.

CRediT authorship contribution statement

N. Babacan: Conceptualization, Methodology, Investigation, Visualization, Writing - original draft, Writing - review & editing. **S. Pauly:** Writing - review & editing. **T. Gustmann:** Conceptualization, Methodology, Investigation, Visualization, Writing - original draft, Writing - review & editing.

Declaration of Competing Interest

The authors declare that they have no known competing financial interests or personal relationships that could have appeared to influence the work reported in this paper.

Acknowledgements

The first author (N. Babacan) gratefully appreciates the support from the Alexander von Humboldt (AvH) Foundation. The authors would like to thank K.-U. Baumgart, N. Geißler, B. Gebel, B. Bartusch, R. Keller, H. Bußkamp and A. Voß for their technical supports. S. Pilz is gratefully acknowledged for fruitful discussions about EBSD analysis as well as J. Hufenbach, U. Kühn and T. Gemming for their persistent scientific support.

References

- J. Mohd Jani, M. Leary, A. Subic, M.A. Gibson, A review of shape memory alloy research, applications and opportunities, *Mater. Des.* 56 (2014) 1078–1113, <https://doi.org/10.1016/j.matdes.2013.11.084>.
- J. Van Humbeeck, Non-medical applications of shape memory alloys, *Mater. Sci. Eng. A* 273–275 (1999) 134–148, [https://doi.org/10.1016/S0921-5093\(99\)00293-2](https://doi.org/10.1016/S0921-5093(99)00293-2).
- M. Vollmer, P. Krooß, C. Segel, A. Weidner, A. Paulsen, J. Frenzel, G. Schaper, G. Eggeler, H. Jürgen, T. Niendorf, Damage evolution in pseudoelastic polycrystalline Co-Ni-Ga high-temperature shape memory alloys, *J. Alloys Compd.* 633 (2015) 288–295, <https://doi.org/10.1016/j.jallcom.2015.01.282>.
- T. Niendorf, P. Krooß, E. Batyrkina, A. Paulsen, Y. Motemani, A. Ludwig, P. Buenconsejo, J. Frenzel, G. Eggeler, H.J. Maier, Functional and structural fatigue of titanium tantalum high temperature shape memory alloys (HT SMAs), *Mater. Sci. Eng. A* 620 (2015) 359–366, <https://doi.org/10.1016/j.msea.2014.10.038>.
- K.K. Mahesh, F.M. Braz Fernandes, G. Gurau, Stability of thermal-induced phase transformations in the severely deformed equiatomic Ni-Ti alloys, *J. Mater. Sci.* 47 (2012) 6005–6014, <https://doi.org/10.1007/s10853-012-6508-x>.
- Y. Sutou, N. Koeda, T. Omori, R. Kainuma, K. Ishida, Effects of ageing on bainitic and thermally induced martensitic transformations in ductile Cu-Al-Mn-based shape memory alloys, *Acta Mater.* 57 (2009) 5748–5758, <https://doi.org/10.1016/j.actamat.2009.08.003>.
- H. Ozcan, J. Ma, S. Wang, I. Karaman, Y.I. Chumlyakov, J. Brown, R.D. Noebe, Effects of cyclic heat treatment and aging on superelasticity in oligocrystalline Fe-Mn-Al-Ni shape memory alloy wires, *Scr. Mater.* 134 (2017) 66–70, <https://doi.org/10.1016/j.scriptamat.2017.02.023>.
- W. Abuzaid, Y. Wu, R. Sidharth, F. Brenne, S. Alkan, M. Vollmer, P. Krooß, T. Niendorf, H. Sehitoglu, FeMnNiAl iron-based shape memory alloy: promises and challenges, *Shape Mem. Superelastic.* 5 (2019) 263–277, <https://doi.org/10.1007/s40830-019-00230-9>.
- T. Tadaki, Cu-based shape memory alloys, in: K. Otsuka, C.M. Wayman (Eds.), *Shape Memory Materials*, Cambridge University Press, Cambridge 1998, pp. 97–116.
- D.C. Lagoudas, *Shape Memory Alloys: Modeling and Engineering Applications*, Springer Science+Business Media LLC, New York, 2008.
- D.D. Gu, W. Meiners, K. Wissenbach, R. Poprawe, Laser additive manufacturing of metallic components: materials, processes and mechanisms, *Int. Mater. Rev.* 57 (3) (2017) 133–164, <https://doi.org/10.1179/1743280411Y.0000000014>.
- S. Saedi, N. Shayesteh, A. Amerinatanzi, M. Elahinia, H.E. Karaca, On the effects of selective laser melting process parameters on microstructure and thermomechanical response of Ni-rich NiTi, *Acta Mater.* 144 (2018) 552–560, <https://doi.org/10.1016/j.actamat.2017.10.072>.
- S. Dadbakhsh, M. Speirs, J.P. Kruth, J. Schrooten, J. Luyten, J. Van Humbeeck, Effect of SLM parameters on transformation temperatures of shape memory nickel titanium parts, *Adv. Eng. Mater.* 16 (2014) 1140–1146, <https://doi.org/10.1002/adem.201300558>.
- T. Gustmann, J.M. dos Santos, U. Kühn, J. Van Humbeeck, S. Pauly, P. Gargarella, Properties of Cu-based shape-memory alloys prepared by selective laser melting, *Shape Mem. Superelastic.* 3 (2016) 24–36, <https://doi.org/10.1007/s40830-016-0088-6>.
- J.P. Oliveira, A.D. LaLonde, J. Ma, Processing parameters in laser powder bed fusion metal additive manufacturing, *Mater. Des.* 193 (2020) 1–12, <https://doi.org/10.1016/j.matdes.2020.108762>.
- J. Ma, B. Franco, G. Tapia, K. Karayagiz, L. Johnson, J. Liu, R. Arroyave, I. Karaman, A. Elwany, Spatial control of functional response in 4D-printed additive metallic structures, *Sci. Rep.* 7 (2017) 1–8, <https://doi.org/10.1038/srep46707>.
- J. Günther, F. Brenne, M. Droste, M. Wendler, O. Volkova, H. Biermann, T. Niendorf, Design of novel materials for additive manufacturing - isotropic microstructure and high defect tolerance, *Sci. Rep.* 8 (2018) 1–14, <https://doi.org/10.1038/s41598-018-19376-0>.
- P. Gargarella, E.M. Mazzer, L.A. Basilio, C. Bolfarini, T. Gustmann, S. Pauly, Phase formation, thermal stability and mechanical properties of a Cu-Al-Ni-Mn shape memory alloy prepared by selective laser melting, *Mater. Res.* 18 (2015) 35–38, <https://doi.org/10.1590/1516-1439.338914>.
- T. Gustmann, A. Neves, U. Kühn, P. Gargarella, C.S. Kiminami, C. Bolfarini, J. Eckert, S. Pauly, Influence of processing parameters on the fabrication of a Cu-Al-Ni-Mn shape-memory alloy by selective laser melting, *Addit. Manuf.* 11 (2016) 23–31, <https://doi.org/10.1016/j.addma.2016.04.003>.
- M.R. da Silva, P. Gargarella, T. Gustmann, W.J. Botta Filho, C.S. Kiminami, J. Eckert, S. Pauly, C. Bolfarini, Laser surface remelting of a Cu-Al-Ni-Mn shape memory alloy, *Mater. Sci. Eng. A* 661 (2016) 61–67, <https://doi.org/10.1016/j.msea.2016.03.021>.
- T. Gustmann, H. Schwab, U. Kühn, S. Pauly, Selective laser remelting of an additively manufactured Cu-Al-Ni-Mn shape-memory alloy, *Mater. Des.* 153 (2018) 129–138, <https://doi.org/10.1016/j.matdes.2018.05.010>.
- J. Tian, W. Zhu, Q. Wei, S. Wen, S. Li, B. Song, Y. Shi, Process optimization, microstructures and mechanical properties of a Cu-based shape memory alloy fabricated by selective laser melting, *J. Alloys Compd.* 785 (2019) 754–764, <https://doi.org/10.1016/j.jallcom.2019.01.153>.
- L. Zhuo, B. Song, R. Li, Q. Wei, C. Yan, Y. Shi, Effect of element evaporation on the microstructure and properties of CuZnAl shape memory alloys prepared by selective laser melting, *Opt. Laser Technol.* 127 (2020) 106164, <https://doi.org/10.1016/j.optlastec.2020.106164>.
- T. Kusama, T. Omori, T. Saito, T. Tanaka, S. Kise, Y. Araki, R. Kinuma, Ultra-large single crystals by abnormal grain growth, *Nat. Commun.* 8 (1–9) (2017) 354.
- S. Xu, T. Kusama, X. Xu, H. Huang, T. Omori, J. Xie, R. Kainuma, Large [001] single crystals via abnormal grain growth from columnar polycrystal, *Materialia* 6 (2019) <https://doi.org/10.1016/j.mta.2019.100336>.
- R. Kainuma, S. Takahashi, K. Ishida, Ductile shape memory alloys of the Cu-Al-Mn system, *J. Phys. IV* 5 (C8) (1995) 961–966, <https://doi.org/10.1051/jp4/199558961>.
- R. Kainuma, S. Takahashi, K. Ishida, Thermoelastic martensite and shape memory effect in ductile Cu-Al-Mn alloys, *Metall. Mater. Trans. A* 27 (1996) 2187–2195.
- T. Kusama, T. Omori, T. Saito, I. Ohnuma, K. Ishida, R. Kainuma, Two- and three-dimensional grain growth in the Cu-Al-Mn shape memory alloy, *Mater. Trans.* 54 (2013) 2044–2048, <https://doi.org/10.2320/matertrans.M2013167>.
- T. Omori, T. Kusama, S. Kawata, I. Ohnuma, Y. Sutou, Y. Araki, K. Ishida, R. Kainuma, Abnormal grain growth induced by cyclic heat treatment, *Science* (80–) 341 (2013) 1500–1502, <https://doi.org/10.1126/science.1238017>.
- T. Kusama, T. Omori, T. Saito, S. Kise, T. Tanaka, Y. Araki, R. Kainuma, Ultra-large single crystal by abnormal grain growth, *Nat. Commun.* (8) 354. doi:<https://doi.org/10.1038/s41467-017-00383-0>.

- [31] S. Yang, F. Zhang, J. Wu, Y. Lu, Z. Shi, C. Wang, X. Liu, Superelasticity and shape memory effect in Cu–Al–Mn–V shape memory alloys, *Mater. Des.* 115 (2017) 17–25, <https://doi.org/10.1016/j.matdes.2016.11.035>.
- [32] S. Yang, J. Zhang, M. Chi, M. Yang, C. Wang, X. Liu, Excellent superelasticity of Cu–Al–Mn–Cr shape memory single crystal obtained only through annealing cast polycrystalline alloy, *Scr. Mater.* 165 (2019) 20–24, <https://doi.org/10.1016/j.scriptamat.2019.02.011>.
- [33] S. Yang, L. Guo, X. Qing, S. Hong, J. Zhang, M. Li, C. Wang, X. Liu, Excellent shape recovery characteristics of Cu–Al–Mn–Fe shape memory single crystal, *J. Mater. Sci. Technol.* 57 (2020) 43–50, <https://doi.org/10.1016/j.jmst.2020.03.076>.
- [34] J.-L. Liu, H.-Y. Huang, J.-X. Xie, The roles of grain orientation and grain boundary characteristics in the enhanced superelasticity of $\text{Cu}_{71.8}\text{Al}_{17.8}\text{Mn}_{10.4}$ shape memory alloys, *Mater. Des.* 64 (2014) 427–433, <https://doi.org/10.1016/j.matdes.2014.07.070>.
- [35] J.-L. Liu, H.-Y. Huang, J.-X. Xie, Superelastic anisotropy characteristics of columnar-grained Cu–Al–Mn shape memory alloys and its potential applications, *Mater. Des.* 85 (2015) 211–220, <https://doi.org/10.1016/j.matdes.2015.06.114>.
- [36] J.-L. Liu, H.-Y. Huang, J.-X. Xie, S. Xu, F. Li, Superelastic fatigue of columnar-grained Cu–Al–Mn shape memory alloy under cyclic tension at high strain, *Scr. Mater.* 136 (2017) 106–110, <https://doi.org/10.1016/j.scriptamat.2017.04.017>.
- [37] W.E. Frazier, Metal additive manufacturing : a review, *J. Mater. Eng. Perform.* 23 (2014) 1917–1928.
- [38] R. Kainuma, Recent progress in shape memory alloys, *Mater. Trans.* 59 (2018) 327–331, <https://doi.org/10.2320/matertrans.M2017340>.
- [39] B. Yuan, X. Zhu, X. Zhang, M. Qian, Elastocaloric effect with small hysteresis in bamboo-grained Cu–Al–Mn microwires, *J. Mater. Sci.* 54 (2019) 9613–9621, <https://doi.org/10.1007/s10853-019-03592-8>.
- [40] H. Wang, H.Y. Huang, Y.J. Su, Tuning the operation temperature window of the elastocaloric effect in Cu–Al–Mn shape memory alloys by composition design, *J. Alloys Compd.* 828 (2020) 154265, <https://doi.org/10.1016/j.jallcom.2020.154265>.
- [41] J. Fiocchi, C.A. Biffi, D. Scaccabarozzi, B. Saggini, A. Tuissi, Enhancement of the damping behavior of $\text{Ti}_6\text{Al}_4\text{V}$ alloy through the use of trabecular structure produced by selective laser melting, *Adv. Eng. Mater.* 22 (2020) 1–6, <https://doi.org/10.1002/adem.201900722>.
- [42] H. Hou, E. Simsek, D. Stasak, N. Al Hasan, S. Qian, R. Ott, J. Cui, I. Takeuchi, Elastocaloric cooling of additive manufactured shape memory alloys with large latent heat, *J. Phys. D: Appl. Phys.* 50 (2017) <https://doi.org/10.1088/1361-6463/aa85bf>.
- [43] J.P. Oliveira, Z. Zeng, T. Omori, N. Zhou, R.M. Miranda, F.M.B. Fernandes, Improvement of damping properties in laser processed superelastic Cu–Al–Mn shape memory alloys, *Mater. Des.* 98 (2016) 280–284, <https://doi.org/10.1016/j.matdes.2016.03.032>.
- [44] K.C. Shrestha, Y. Araki, T. Nagae, Y. Koetaka, Y. Suzuki, T. Omori, Y. Sutou, R. Kainuma, K. Ishida, Feasibility of Cu–Al–Mn superelastic alloy bars as reinforcement elements in concrete beams, *Smart Mater. Struct.* 22 (2013), 025025, <https://doi.org/10.1088/0964-1726/22/2/025025>.
- [45] T. Omori, J. Wang, Y. Sutou, R. Kainuma, K. Ishida, Two-way shape memory effect induced by bending deformation in ductile Cu–Al–Mn alloys, *Mater. Trans.* 43 (2002) 1676–1683, <https://doi.org/10.2320/matertrans.43.1676>.
- [46] J.P. Oliveira, B. Pantón, Z. Zeng, T. Omori, Y. Zhou, R.M. Miranda, F.M. Braz Fernandes, Laser welded superelastic Cu–Al–Mn shape memory alloy wires, *Mater. Des.* 90 (2016) 122–128, <https://doi.org/10.1016/j.matdes.2015.10.125>.
- [47] J.P. Oliveira, Z. Zeng, C. Andrei, F.M.B. Fernandes, R.M. Miranda, A.J. Ramirez, T. Omori, N. Zhou, Dissimilar laser welding of superelastic NiTi and CuAlMn shape memory alloys, *Mater. Des.* 128 (2017) 166–175, <https://doi.org/10.1016/j.matdes.2017.05.011>.
- [48] D. Herzog, V. Seyda, E. Wycisk, C. Emmelmann, Additive manufacturing of metals, *Acta Mater.* 117 (2016) 371–392, <https://doi.org/10.1016/j.actamat.2016.07.019>.
- [49] S. Vock, B. Klöden, A. Kirchner, T. Weißgärber, B. Kieback, Powders for powder bed fusion: a review, *Prog. Addit. Manuf.* 4 (2019) 383–397, <https://doi.org/10.1007/s40964-019-00078-6>.
- [50] T. Gustmann, F. Guttmann, F. Wenz, P. Koch, R. Stelzer, W.G. Drossel, H. Korn, Properties of a superelastic NiTi shape memory alloy using laser powder bed fusion and adaptive scanning strategies, *Prog. Addit. Manuf.* 5 (2020) 11–18, <https://doi.org/10.1007/s40964-020-00118-6>.
- [51] C. Haberland, M. Elahinia, J.M. Walker, H. Meier, J. Frenzel, On the development of high quality NiTi shape memory and pseudoelastic parts by additive manufacturing, *Smart Mater. Struct.* 23 (2014) 104002, <https://doi.org/10.1088/0964-1726/23/10/104002>.
- [52] T. Gustmann, A. Neves, U. Kühn, P. Gargarella, C.S. Kiminami, C. Bolfarini, J. Eckert, S. Pauly, Fabrication of Cu–Al–Ni–Mn shape-memory parts by selective laser melting, in: B. Müller (Ed.), *Fraunhofer Direct Digital Manufacturing Conference 2016*, pp. 159–164.
- [53] S. Leuders, S. Meiners, L. Wu, A. Taube, T. Tröster, T. Niendorf, Structural components manufactured by selective laser melting and investment casting—impact of the process route on the damage mechanism under cyclic loading, *J. Mater. Process. Technol.* 248 (2017) 130–142, <https://doi.org/10.1016/j.jmatprotec.2017.04.026>.
- [54] G.M. Karthik, P. Sathiyamoorthi, A. Zargaran, J.M. Park, P. Asghari-Rad, S. Son, S.H. Park, H.S. Kim, Novel precipitation and enhanced tensile properties in selective laser melted Cu–Sn alloy, *Materialia* 13 (2020) 100861, <https://doi.org/10.1016/j.mta.2020.100861>.
- [55] T. Bormann, R. Schumacher, B. Müller, M. Mertmann, M. De Wild, Tailoring selective laser melting process parameters for NiTi implants, *J. Mater. Eng. Perform.* 21 (2012) 2519–2524, <https://doi.org/10.1007/s11665-012-0318-9>.
- [56] X. Wang, S. Kustov, J. Van Humbeeck, A short review on the microstructure, transformation behavior and functional properties of NiTi shape memory alloys fabricated by selective laser melting, *Materials (Basel)* 11 (2018) 1683, <https://doi.org/10.3390/ma11091683>.
- [57] Y. Sutou, T. Omori, R. Kainuma, K. Ishida, Ductile Cu–Al–Mn based shape memory alloys: general properties and applications, *Mater. Sci. Technol.* 24 (2008) 896–901, <https://doi.org/10.1179/174328408X302567>.
- [58] N. Babacan, J. Ma, O.S. Turkbak, I. Karaman, B. Kockar, The effects of cold rolling and the subsequent heat treatments on the shape memory and the superelasticity characteristics of $\text{Cu}_{73}\text{Al}_{16}\text{Mn}_{11}$ shape memory alloy, *Smart Mater. Struct.* 27 (2018), 015028, .
- [59] N. Babacan, K.C. Atli, O.S. Turkbak, I. Karaman, B. Kockar, The effect of dynamic aging on the cyclic stability of $\text{Cu}_{73}\text{Al}_{16}\text{Mn}_{11}$ shape memory alloy, *Mater. Sci. Eng. A* 701 (2017) 352–358, <https://doi.org/10.1016/j.msea.2017.06.104>.
- [60] Y. Yang, J.B. Zhan, Z.Z. Sun, H.L. Wang, J.X. Lin, Y.J. Liu, L.C. Zhang, Evolution of functional properties realized by increasing laser scanning speed for the selective laser melting fabricated NiTi alloy, *J. Alloys Compd.* 804 (2019) 220–229, <https://doi.org/10.1016/j.jallcom.2019.06.340>.
- [61] C. Lauhoff, A. Fischer, C. Sobrero, M. Kahlert, S. Bo, Additive manufacturing of Co–Ni–Ga high-temperature shape memory alloy: processability and phase transformation behavior, *Metall. Mater. Trans. A* 51 (2020) 1056–1061.
- [62] T. Niendorf, S. Leuders, A. Riemer, F. Brenne, T. Tröster, H.A. Richard, D. Schwarze, Functionally graded alloys obtained by additive manufacturing, *Adv. Eng. Mater.* 16 (2014) 857–861, <https://doi.org/10.1002/adem.201300579>.
- [63] S. Saedi, A.S. Turabi, M.T. Andani, N.S. Moghaddam, M. Elahinia, H.E. Karaca, Texture, aging, and superelasticity of selective laser melting fabricated Ni-rich NiTi alloys, *Mater. Sci. Eng. A* 686 (2017) 1–10, <https://doi.org/10.1016/j.msea.2017.01.008>.
- [64] T. Niendorf, F. Brenne, P. Krooß, M. Vollmer, J. Günther, D. Schwarze, H. Biermann, Microstructural evolution and functional properties of Fe–Mn–Al–Ni shape memory alloy processed by selective laser melting, *Metall. Mater. Trans. A* 47 (2016) 2569–2573, <https://doi.org/10.1007/s11661-016-3412-z>.
- [65] L.N. Carter, C. Martin, P.J. Withers, M.M. Attallah, The influence of the laser scan strategy on grain structure and cracking behaviour in SLM powder-bed fabricated nickel superalloy, *J. Alloys Compd.* 615 (2014) 338–347, <https://doi.org/10.1016/j.jallcom.2014.06.172>.
- [66] R. Santamarta, C. Seguí, J. Pons, Martensite stabilization in $\text{Ni}_{50}\text{Ti}_{32.2}\text{Hf}_{17.7}$, *Scr. Mater.* 41 (1999) 867–872.
- [67] Y. Wang, C. Huang, J. Gso, S. Yang, X. Ding, X. Song, X. Ren, Evidence for ferromagnetic strain glass in Ni–Co–Mn–Ga Heusler alloy system, *Appl. Phys. Lett.* 101 (2012) 101913.
- [68] X. Sun, D. Cong, Y. Ren, K.D. Liss, D.E. Brown, Z. Ma, S. Hao, W. Xia, Z. Chen, L. Ma, X. Zhao, Z. He, J. Liu, R. Li, Y. Wang, Magnetic-field-induced strain-glass-to-martensite transition in a Fe–Mn–Ga alloy, *Acta Mater.* 183 (2020) 11–23, <https://doi.org/10.1016/j.actamat.2019.10.051>.
- [69] C. Lexcelent, B.C. Goo, Q.P. Sun, J. Bernardini, Characterization, thermomechanical behaviour and micromechanical-based constitutive model of shape-memory Cu–Zn–Al single crystals, *Acta Mater.* 44 (1996) 3773–3780, [https://doi.org/10.1016/1359-6454\(95\)00452-1](https://doi.org/10.1016/1359-6454(95)00452-1).
- [70] U.S. Mallik, V. Sampath, Influence of aluminum and manganese concentration on the shape memory characteristics of Cu–Al–Mn shape memory alloys, *J. Alloys Compd.* 459 (2008) 142–147, <https://doi.org/10.1016/j.jallcom.2007.04.254>.
- [71] C. Aksu Canbay, Z. Karagoz, F. Yakuphanoglu, Controlling of transformation temperatures of Cu–Al–Mn shape memory alloys by chemical composition, *Acta Phys. Pol. A* 125 (2014) 1163–1166, <https://doi.org/10.12693/APhysPolA.125.1163>.
- [72] Y. Chen, C.A. Schuh, Size effects in shape memory alloy microwires, *Acta Mater.* 59 (2011) 537–553, <https://doi.org/10.1016/j.actamat.2010.09.057>.
- [73] Y. Sutou, T. Omori, K. Yamauchi, N. Ono, R. Kainuma, K. Ishida, Effect of grain size and texture on pseudoelasticity in Cu–Al–Mn-based shape memory wire, *Acta Mater.* 53 (2005) 4121–4133, <https://doi.org/10.1016/j.actamat.2005.05.013>.
- [74] P. La Roca, L. Isola, P. Vermaut, J. Malarria, Relationship between grain size and thermal hysteresis of martensitic transformations in Cu-based shape memory alloys, *Scr. Mater.* 135 (2017) 5–9, <https://doi.org/10.1016/j.scriptamat.2017.03.016>.
- [75] M. Speirs, X. Wang, S. Van Baelen, A. Ahadi, S. Dadbakhsh, J.P. Kruth, J. Van Humbeeck, On the transformation behavior of NiTi shape-memory alloy produced by SLM, *Shape Mem. Superelastic.* 2 (2016) 310–316, <https://doi.org/10.1007/s40830-016-0083-y>.
- [76] X. Wang, J. Yu, J. Liu, L. Chen, Q. Yang, H. Wei, J. Sun, Z. Wang, Z. Zhang, G. Zhao, J. Van Humbeeck, Effect of process parameters on the phase transformation behavior and tensile properties of NiTi shape memory alloys fabricated by selective laser melting, *Addit. Manuf.* 36 (2020) 101545, <https://doi.org/10.1016/j.addma.2020.101545>.
- [77] M. Mahmoudi, G. Tapia, B. Franco, J. Ma, R. Arroyave, I. Karaman, A. Elwany, On the printability and transformation behavior of nickel-titanium shape memory alloys fabricated using laser powder-bed fusion additive manufacturing, *J. Manuf. Process.* 35 (2018) 672–680, <https://doi.org/10.1016/j.jmapro.2018.08.037>.
- [78] P. La Roca, L. Isola, P. Vermaut, J. Malarria, Relationship between martensitic plate size and austenitic grain size in martensitic transformations, *Appl. Phys. Lett.* 106 (2015) 221903.
- [79] Y. Sutou, T. Omori, N. Koeda, R. Kainuma, K. Ishida, Effects of grain size and texture on damping properties of Cu–Al–Mn-based shape memory alloys, *Mater. Sci. Eng. A* 438–440 (2006) 743–746, <https://doi.org/10.1016/j.msea.2006.02.085>.
- [80] K. Otsuka, X. Ren, Mechanism of martensite aging effect, *Scr. Mater.* 50 (2004) 207–212.
- [81] T. Riipinen, S. Metsä-Kortelainen, T. Lindroos, J.S. Keränen, A. Manninen, J. Pippuri-Mäkeläinen, Properties of soft magnetic Fe–Co–V alloy produced by laser powder bed fusion, *Rapid Prototyp. J.* 25 (2019) 699–707, <https://doi.org/10.1108/RPJ-06-2018-0136>.